Carbon 122 (2017) 710–717

Contents lists available at ScienceDirect

Carbon

journal homepage: www.elsevier.com/locate/carbon

Nickel nanoparticles partially embedded into carbon fiber cloth via metal-mediated pitting process as flexible and efficient electrodes for hydrogen evolution reactions

Linjing Yang [a], Weijia Zhou [a, *], Jin Jia [a], Tanli Xiong [a], Kai Zhou [a], Chunhua Feng [a], Jian Zhou [b], Zhenghua Tang [a], Shaowei Chen [a, c]

[a] New Energy Research Institute, Guangdong Provincial Key Laboratory of Atmospheric Environment and Pollution Control, School of Environment and Energy, South China University of Technology, Guangzhou Higher Education Mega Center, Guangzhou, Guangdong, 510006, China
[b] National Laboratory of Solid State Microstructures and Department of Materials Science and Engineering, Nanjing University, Nanjing, Jiangsu 210093, China
[c] Department of Chemistry and Biochemistry, University of California, 1156 High Street, Santa Cruz, CA 95064, United States

ARTICLE INFO

Article history:
Received 5 March 2017
Received in revised form
4 July 2017
Accepted 10 July 2017
Available online 12 July 2017

ABSTRACT

Sunlight-driven electrolytic splitting of water is a promising route to hydrogen production, and widespread implementation has called for the development of inexpensive, robust and large-scale electrodes. Here, nickel nanoparticles partially embedded into carbon fiber cloth (NiΦCFC) is prepared on a large scale (e.g., 40 cm × 40 cm) via a metal-mediated pitting process, which is adopted to fabricate hydrogen evolution reaction electrode for the first time. The partially embedded structure is beneficial for regulating the electron density state of carbon, exposing the nickel catalytic sites and improving the catalytic stability. The two kinds of electrochemical area and density functional theory results confirm that the interface effect between nickel and defective carbon leads into a low Gibbs free energy of H* adsorption. The NiΦCFC as flexible and efficient electrodes require a small overpotential of 131.5 mV to achieve −10 mA cm^{-2}. Note that the two-electrode electrolyzer composed of FeNi layered double hydroxide loaded on CFC (NiFe-LDH/CFC) (+)//NiΦCFC (−) possesses a voltage of 1.54 V at −10 mA cm^{-2}, which can also be powered by a solar cell. The facile and large-scale preparation of NiΦCFC as flexible electrodes could be adapted for the industrial hydrogen production powered by solar energy.

1. Introduction

With the increasing energy crisis, hydrogen has been considered to be one of the most promising candidates for replacing fossil fuel energy. As a well-established technology for energy conversion, electrochemical water splitting offers a simple and promising approach for the hydrogen evolution reaction (HER) [1–4]. Alkaline water splitting has already been used in commercial applications for the mass production of hydrogen. Ni-based compounds, such as Ni@Cr_2O_3-NiO [5], NiMo hollow nanorod array [6], nickel oxide/nickel heterostructures on carbon nanotubes (NiO/Ni-CNT) [7], and NiFe/nickel foam [8], have been extensively studied as efficient and stable non-noble metal catalysts for water splitting in alkaline solutions. For example, Sun et al. [9] reported an ultrathin single-crystalline Ni nanosheet array via in situ topotactic reduction from $Ni(OH)_2$ array, which exhibited substantially enhanced activity and stability towards effective water splitting. However, the preparation of large size and inexpensive electrodes with high catalytic activity and stability for water splitting remains challenging.

The loading of electrocatalyst on conductive substrates (e.g., graphene sheets, carbon nanotubes and carbon paper) can significantly improve the cycling stability for HER due to efficient charge transport [7,10,11]. However, the interface between electrocatalysts and carbon substrates was limited and the nanoparticles tend to peel off the substrate due to vigorous gas evolution. To solve this problem, recently, novel HER systems of metals@carbon core-shell structure (e.g., Co@N-doped C, Fe@C, CoNi@N-doped C and Au@N-doped C) have been widely reported [12–17]. For example, Bao et al. [12] reported that CoNi alloy particles wrapped in ultrathin graphene layers significantly increased the interface effect between

* Corresponding author.
E-mail address: eszhouwj@scut.edu.cn (W. Zhou).

http://dx.doi.org/10.1016/j.carbon.2017.07.027
0008-6223/

metal core and carbon shell to enhance the HER activity. The thickness of the carbon shell is difficult to control precisely during the preparation process, which should not be thicker than 2 nm. Therefore, maximally expose the catalytic sites and fully expand the interfacial interaction between the electrocatalyst and conductive substrate is valuable and remains urgent for promoting the water splitting [18]. To solve such issue, the catalysts have been embedded into nanoholes, and the active catalytic sites were exposed. For example, Shan and Chen et al. reported the Pt nanoparticles were anchored into oxide nanotraps via strong metal–oxide interactions while still leaving active metal facets exposed, which caused the enhancement of thermal stability and activity of precious metal NPs [19].

Herein, a novel model consisting of Ni nanoparticles partially embedded in carbon fiber cloth (NiΦCFC) was proposed, which was prepared via a metal-mediated pitting process. The metal-mediated pitting process is a well-known one in engineering to obtain porous graphene [20] and graphene nanobelts [21], but adopted to fabricate metal@carbon HER electrodes for the first time. The embedded Ni nanoparticles into CFC are beneficial for regulating the electron density state of carbon, exposing the Ni catalytic sites and improving the catalytic stability. The obtained NiΦCFC was used as a flexible cathode and exhibited remarkable high catalytic activity for the HER, which required an overpotential of only 131.5 mV to obtain a current density of -10 mA cm^{-2} with a Tafel slope of 123.4 mV dec^{-1} and strong catalytic stability in 1 M KOH with a large current density of -147.2 mA cm^{-2} for 113.8 h. Furthermore, density functional theory (DFT) results revealed that the Ni embedded in the carbon possessed a lower Gibbs free energy of H* adsorption ($|\Delta GH^*|$), particularly for the para carbon atoms. Notably, the alkaline water electrolyzer using NiΦCFC as the cathode and NiFe-LDH/CFC as an anode afforded a water-splitting current density of -10 mA cm^{-2} at a voltage of 1.54 V, which lasted for 33 h without decay.

2. Experimental

2.1. Chemicals

Nickel (II) acetate tetrahydrate ($NiC_4H_6O_4\cdot 4H_2O$) and ferric (III) nitrate nonahydrate ($Fe(NO_3)_3\cdot 9H_2O$) were purchased from Sinopharm Chemical Reagents Beijing Co. All of the reagents were of analytical grade and used without further treatment. The carbon fiber cloth (CFC) was purchased from CeTech Co., Ltd., China. Deionized (D.I.) water was purified using a Milli-Q system (Millipore, Billerica, USA).

2.2. Preparation of Ni nanoparticles partially embedded in carbon fiber cloth (NiΦCFC)

Carbon fiber cloth (Fig. S1) was firstly cleaned by 1 M H_2SO_4, ethanol and distilled water, respectively, combined with ultrasonic treatment. Briefly, $NiC_4H_6O_4\cdot 4H_2O$ (2 g) was dissolved in D.I. water (40 mL); then, a 3 cm × 3 cm (or 40 cm × 40 cm) piece of CFC was added to this aqueous solution to adsorb Ni ions for 12 h. Next, the CFC with Ni ions was freeze-dried to yield $Ni(OH)_2$/CFC [22]. The obtained $Ni(OH)_2$/CFC was calcined at 900 °C for 3 h under a gas mixture that consisted of 10% H_2/Ar to obtain Ni nanoparticles that were partially embedded in the CFC (NiΦCFC). The Ni loading amount was confirmed to be about 2.52 mg cm^{-2} by acid dissolution and 18.6 wt% by thermogravimetric analysis (Fig. S2). The Ni content in NiΦCFC can be controlled by different loading amount of $Ni(OH)_2$ on CFC (Fig. S3). The blank sample, Ni nanoparticles loaded on CFC (Ni/CFC), was synthesized using a similar process at a lower calcination temperature (such as 600 °C).

2.3. Characterizations

Field-emission scanning electron microscopic (FESEM, Model JSM-7600F) measurements were employed to characterize the morphologies of the obtained samples. Powder X-ray diffraction (XRD) patterns of the samples were recorded with a Bruke D8 Advance powder X-ray diffractometer with Cu Kα (λ = 0.15406 nm) radiation. Transmission electron microscopy (TEM, JEOL 2100F) equipped with an energy dispersive X-ray spectrometer (EDS). The Ni nanoparticles were removed from NiΦCFC via sonication. X-ray photoelectron spectroscopic (XPS) measurements were performed using a PHI X-tool instrument (Ulvac-Phi). Raman spectra were recorded on a RENISHAW in Via instrument with an Ar laser source of 488 nm in a macroscopic configuration. Thermogravimetric analysis (TGA) was performed with a TGA/DSC1 Mettler-Toledo thermal analyzer at a heating rate of 5 °C min^{-1} in a stream of oxygen (50 mL min^{-1}).

2.4. Electrochemistry

Electrochemical measurements were performed with an electrochemical workstation (EW, Solartron Analytical 1287 + 1260) in a 1 M KOH aqueous solution. A saturated calomel electrode (Hg/Hg_2Cl_2 in saturated KCl) and a carbon rod were used as the reference and counter electrode, respectively. The tailored NiΦCFC (1.0 cm × 2.0 cm) was used as cathode for HER. The saturated calomel electrode was calibrated with respect to a reversible hydrogen electrode (RHE, Fig. S4). Polarization curves without and with ohmic compensation for HER were acquired by sweeping the potential from -0.8 to -1.6 V (vs. SCE) at a potential sweep rate of 5 mV s^{-1}. The tailored NiFe-LDH/CFC (1.0 cm × 2.0 cm) was used as anode for OER. Polarization curves without ohmic compensation for OER were acquired by sweeping the potential from 0 to 0.9 V (vs. SCE) at a potential sweep rate of 5 mV s^{-1}. Electrochemical impedances of electrodes were carried out with an amplitude of 10 mV and frequency range from 100 kHz to 0.01 Hz. Cyclic voltammetry (CV) was used to probe the electrochemical double layer capacitance (DLC) in nonfaradaic potential window to estimate the effective electrode surface area of CFC and the pseudocapacitance (PC) of Ni nanoparticles in a faradaic potential window. Current-time responses were monitored by chronoamperometric measurements by the four different overpotentials of 115 mV, 215 mV, 315 mV and 515 mV for 48 h, 48 h, 16.5 h and 113.8 h, respectively. The electrolytic tank was sealed by sealing film and the gas mixture of hydrogen and oxygen was accumulated with the reaction time and collected by a microsyringe every 1 h. The hydrogen and oxygen have the different peak positions in gas chromatography (GC-2060) due to the different molecular weights. The H_2 production was calculated according to the formula $V(H_2) = S_t/S_s \times V/(22.4 \times t)$, where S_t was the peak area of H_2 tested by GC for 1 mL gas collected from the sealed cell, S_s was the peak area tested by 1 mL pure hydrogen (99.9%), V was the volume of the electrolytic tank minus that of the electrolyte, and t was the test time.

2.5. Two-electrode electrolysis of water driven by solar cell

A commercial polycrystalline silicon thin film solar cell with a maximum voltage of 2.00 V was driven by a Xe lamp with the light intensity of 49.2 mW cm^{-2} and sunlight at noon. The solar cell, a two-electrode electrolyzer with an anion exchange membrane (Zhejiang Qianqiu Group Co., Ltd., China.) and an EW were connected in series. NiΦCFC (1.0 cm × 2.0 cm) and NiFe-LDH/CFC (1.0 cm × 2.0 cm) were used as the cathode and anode to produce H_2 and O_2 in a 1 M KOH aqueous solution, respectively. By connecting the electrolyzer, solar cells and electrochemical workstation

(EW) in series, the polarization curves were obtained in the dark and under light illumination by a solar cell. Polarization curves without ohmic compensation were acquired at a potential sweep rate of 5 mV s^{-1}. Chronopotentiometry curves of the electrolyzer with NiΦCFC and NiFe-LDH/CFC driven by solar cell in the light and with a constant voltage of 2 V from EW in dark, respectively.

2.6. DFT calculations

The calculations were performed using the density functional theory (DFT) as implemented in the Vienna Ab Initio Simulation Package (VASP) [23,24] and the projected augmented wave method [25,26] and the Perdew-Burke-Ernzerhof exchange-correlation function [27] were used. A ($4 \times 4 \times 1$) graphene supercell with a vacuum layer of 15 Å was constructed to simulate a small carbon defect by removing 2 carbon atoms. In addition, we used a larger supercell ($5 \times 5 \times 1$) to simulate a large defect with 4 carbon atoms removed from the structure. The Brillouin zone integration was performed on a Γ-center $5 \times 5 \times 1$ k-point mesh, and the Gaussian smearing width was 0.05 eV. The cutoff energy was 400 eV during the calculation. The atomic positions were fully optimized until the maximum residual forces of all of the atoms were less than 0.02 eV/Å. An effective Hubbard U of 5.0 eV was used for the Ni element. The Gibbs free energy of hydrogen absorption (ΔG_H) was calculated as follows: $\Delta G_H = \Delta E_H + 0.24$ eV, where $\Delta E_H = E_{M+H} - E_M - 1/2\ E_{H2}$ (E_{M+H} is the total energy of the Ni-doped graphene with a single hydrogen atom absorbed on the surface, E_M is the total energy of the Ni-doped graphene without hydrogen atom, and E_{H2} is the total energy of a hydrogen molecule in the gas phase) [28].

3. Results and discussion

A schematic diagram of the typical preparation process for Ni/CFC and NiΦCFC is shown in Fig. 1. First of all, the Ni^{2+} ions are adsorbed onto the CFC followed by transformation into $Ni(OH)_2$/CFC from freeze-dried $NiC_4H_6O_4$ (Fig. 1a and Fig. S5) [29]. Second, the Ni nanoparticles (10–100 nm) on the surface of the CFC were formed by thermal reduction of $Ni(OH)_2$ nanosheets by 10% H_2/Ar at 600 °C (Ni/CFC) (Fig. 1b and Fig. S6). Third, the etching reaction between the Ni nanoparticles and CFC was carried out at 900 °C (Fig. 1c). As shown in SEM images (Fig. 2a–c), the Ni nanoparticles with increased sizes of 100–300 nm were evenly embedded onto the CFC surface (Fig. 2b). The Ni nanoparticles decomposed the C–C bonds to produce free carbon atoms, which were blown away by an Ar/H_2 gas flow. A significant amount of holes were formed on the surface of the CFC. The cross-section of NiΦCFC demonstrated the porous structure of CFC (Fig. 2c), beneficial to the infiltration of the electrolyte. However, at the lower etching temperature, such as 800 °C, the etching can be also carried out, but need longer time (Fig. S7). The elemental mapping analysis (Fig. 2d) indicated that a large number of Ni nanoparticles as discrete points embedded onto the entire basal plane of the CFC and a uniform distribution of numerous C and O. It is important to note that the obtained NiΦCFC still possessed good flexibility (inset of Fig. 2a) and could be folded continuously. The synthesis process of flexible NiΦCFC is quite simple and can be easily scaled up, such as 40 cm × 40 cm (Fig. S8).

The XRD patterns of the CFC and NiΦCFC were shown in Fig. 2e. The peak at approximately 25.3°and 43.3° corresponding to (002) and (100) facets (JCPDS no. 41-1487) were indexed to the orderly stacked graphene of the CFC. The other peaks located at 44.7°, 51.8° and 76.2° were attributed to the (111), (200) and (220) planes of metallic Ni (JCPDS no. 04-0850). Raman spectra for the CFC and NiΦCFC indicated that the metal etching process produced a large quantity of edge defects in the graphene. The I_D/I_G intensity ratio increased from 1.48 of CFC to 1.96 for NiΦCFC (Fig. 2f). In addition to the two peaks, four Raman peaks for Ni-O binding in NiΦCFC at 243.2, 477.8, 605.3, and 995.1 cm^{-1} were observed, due to the surface oxidation of Ni nanoparticles.

The Ni nanoparticles with a size of ~300 nm removed from NiΦCFC were characterized by the transmission electron microscopy (TEM, Fig. 3a). A discontinuous and amorphous $Ni(OH)_2$ layer with a thickness of 3–5 nm was observed on the surface of the Ni nanoparticle (inset of Fig. 3a). The core exhibited an obvious crystal lattice with an interplanar spacing of 0.204 nm, corresponding to (111) of body-centered cubic Ni (Fig. 3b). The distributions of O and Ni elements from the elemental mapping also confirmed the similar conclusion (Fig. 3c). Consistent results can be found in X-ray photoelectron spectroscopy (XPS) spectra of NiΦCFC. The Ni 2p spectrum can be fitted to two spin-orbit peaks (i.e., Ni $2p_{1/2}$ at 873 eV and Ni $2p_{3/2}$ at 855.4 eV) with two shakeup satellites,

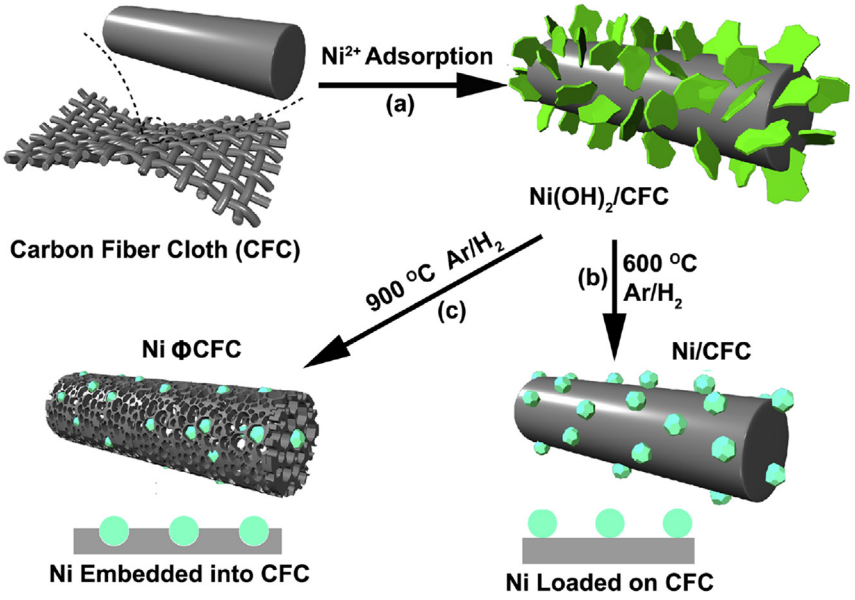

Fig. 1. The synthetic procedure of (a) $Ni(OH)_2$/CFC, (b) Ni/CFC and (c) NiΦCFC. (A colour version of this figure can be viewed online.)

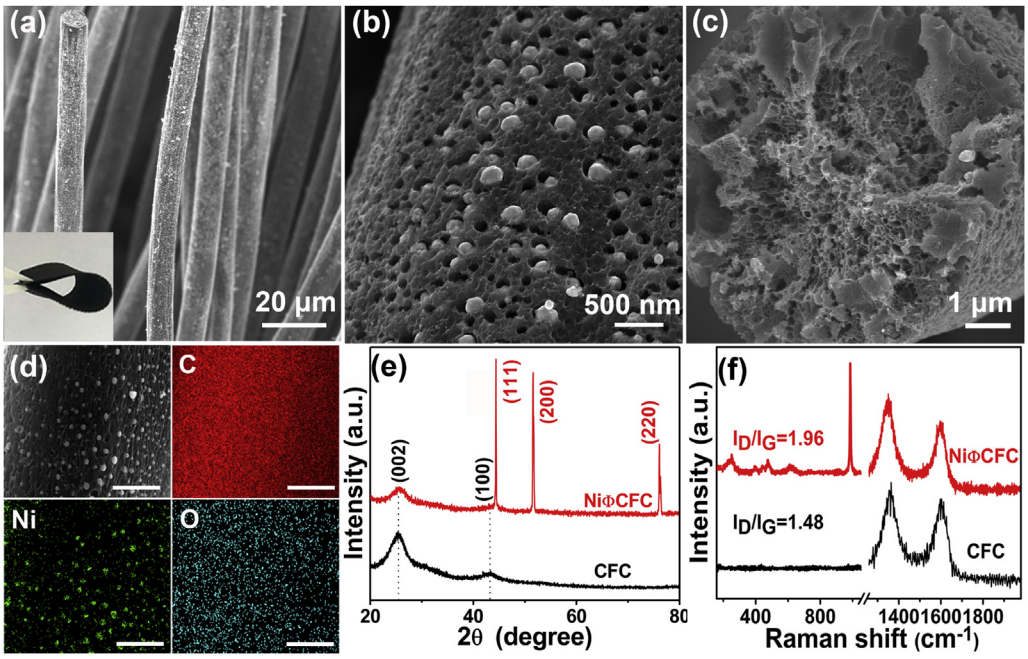

Fig. 2. SEM images (a–c), EDX elemental mapping (d), XRD pattern (e) and Raman spectra (f) of NiΦCFC and CFC. Inset in Fig. 2a is an image of the flexible NiΦCFC. (A colour version of this figure can be viewed online.)

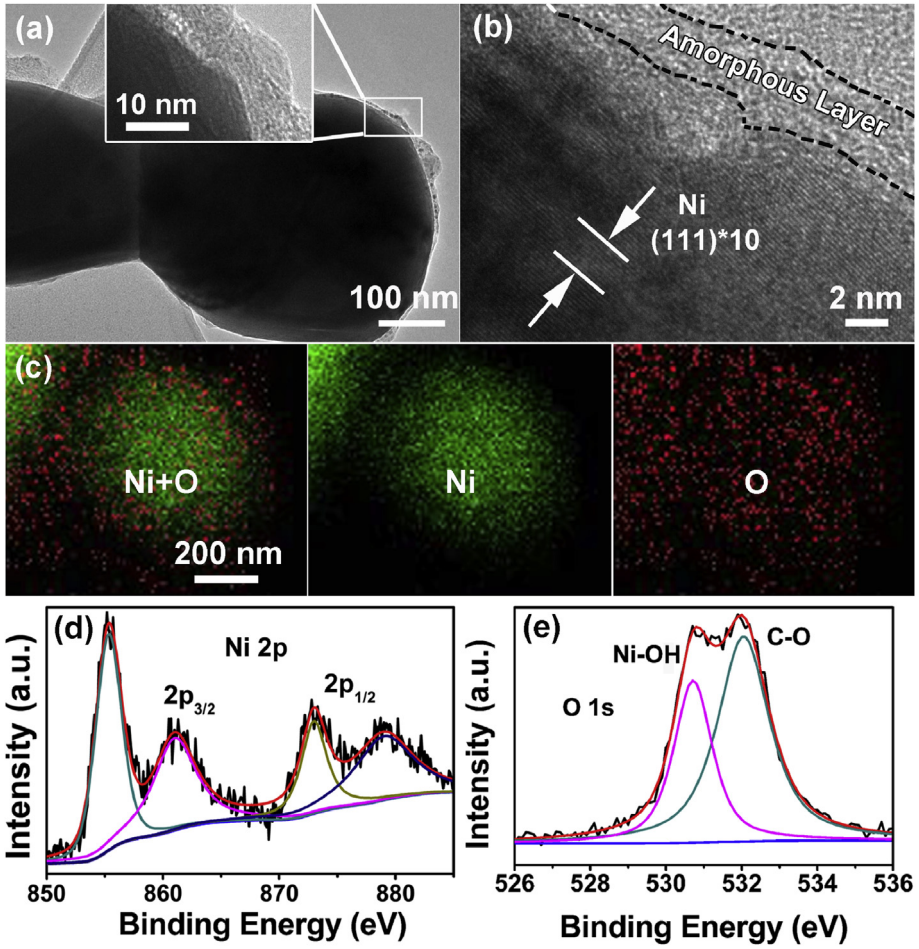

Fig. 3. (a, b) High-resolution TEM images and (c) elemental mapping result for the Ni nanoparticle from NiΦCFC. High-resolution XPS spectra of Ni 2p (d) and O 1s (e) in NiΦCFC. (A colour version of this figure can be viewed online.)

indicating the Ni 2p oxidation state of Ni due to the amorphous nickel hydroxide layer (Fig. 3d) [30]. Fig. 3e showed the two deconvoluted peaks of O 1s at 531.1 eV and 532.1 eV due to Ni-OH for the Ni nanoparticles and C-O for the CFC, respectively [31].

The obtained NiΦCFC (obtained at 900 °C) as a flexible cathode, as well as the control samples (i.e., NF-600, NF-900, CFC-600, CFC-900, Ni/CFC obtained at 600 °C and 20 wt% Pt/C), were evaluated using a three-electrode system in 1 M KOH (Fig. 4a). First, NiΦCFC possessed lower onset potential of −32.8 mV vs. RHE (achieve −1 mA cm^{-2}, Fig. S9a), which was much better than Ni/CFC (−87.8 mV). The two samples had the same crystal structure (XRD, Fig. 2e and Fig. S6), valence state (XPS, Fig. 3d, e and Fig. S6), and similar content (16.6 wt % vs. 17.1 wt%) of Ni nanoparticles, which didn't affect HER performance between them. Second, the size of Ni in NiΦCFC (100–300 nm) is much larger than that of Ni/CFC (10–100 nm), and increased size usually caused the reduced catalytic activity. Third, in order to confirm the effect of calcination temperature on catalytic activity of Ni and CFC, the nickel foam (NF) and CFC were calcined at 600 °C and 900 °C under a gas mixture of 10% H_2/Ar, which were named as NF-600, NF-900, CFC-600 and CFC-900, respectively. The four samples at the current density of −10 mA cm^{-2} possessed the overpotential of −311.7 mV vs. RHE (NF-600), −315.9 mV (NF-900), −547.8 mV (CFC-600), and −542.9 mV (CFC-900), which confirmed the calcination temperature didn't significantly affect the HER activity. In addition, the NiΦCFC also possessed the lower overpotential of 131.5 mV (achieve −10 mA cm^{-2}) than those of Ni/CFC (186.6 mV), and close to that of 20 wt% Pt/C (50.8 mV), as shown in Fig. S9a.

The Tafel slope revealed the inherent reaction processes of the HER, and the Tafel slope of NiΦCFC (123.4 mV dec^{-1}) was smaller than those of NF-600 (131.4 mV dec^{-1}), NF-900 (127.6 mV dec^{-1}) and Ni/CFC (138.1 mV dec^{-1}), but larger than that of 20 wt% Pt/C (31.8 mV dec^{-1}) (Fig. 4b). The Nyquist plots and the equivalent circuit of the NiΦCFC electrodes also suggested a fast electron transfer and consequently facile HER kinetics at the electrocatalyst/electrolyte interface (Fig. S10). In addition, after iR-correction by impedance value, the polarization curves of NiΦCFC were given in Fig. S9b implying the high electronic conductivity of NiΦCFC.

The surface structure of NiΦCFC can be divided into three parts, including the Ni nanoparticles, CFC and interface between Ni nanoparticles and CFC. To fully elucidate the mechanism of enhanced catalytic activity for NiΦCFC, the two types of electrochemical areas were measured including the electric double layer capacitance (DLC) of the CFC and the pseudocapacitance (PC) of the Ni nanoparticles. Cyclic voltammetry (CV) was used to measure the DLC (proportional to r, r is the sweep speed) and PC (proportional to $r^{1/2}$) at the solid-

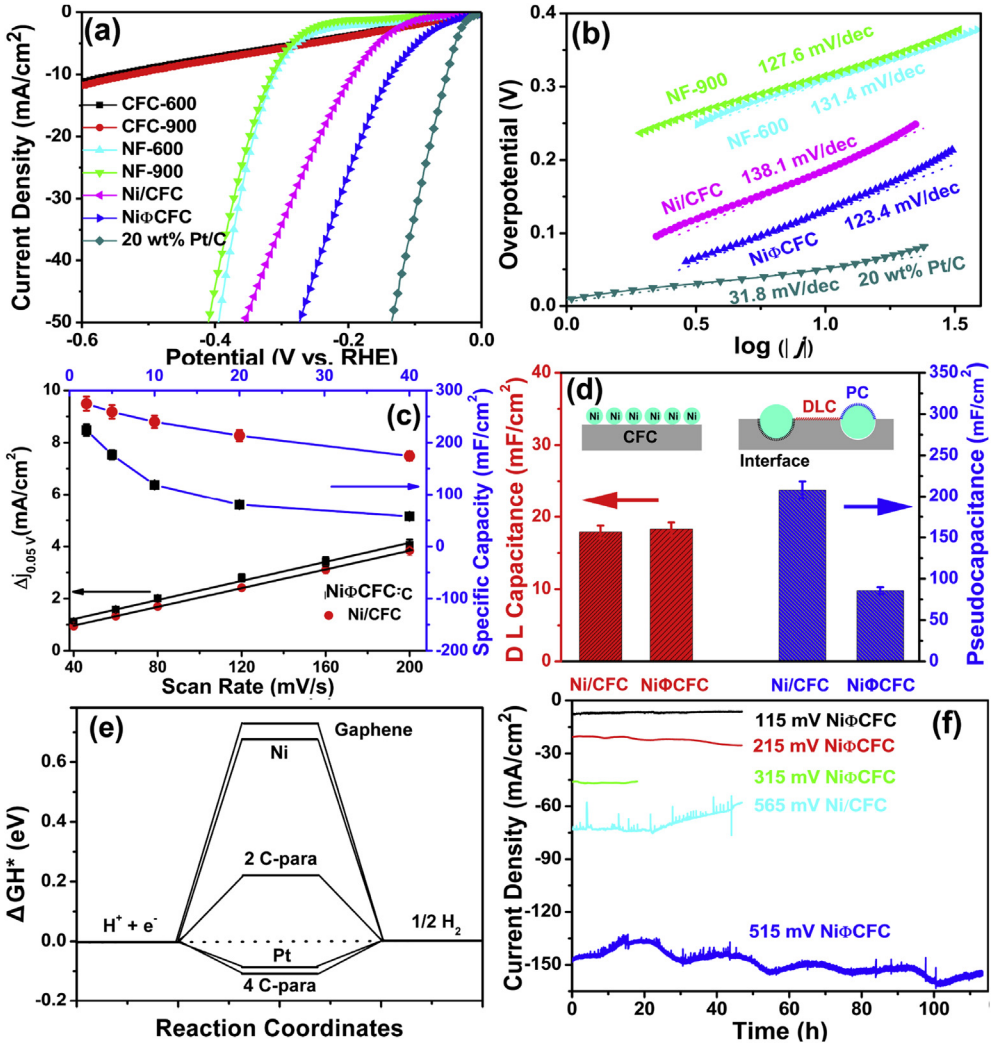

Fig. 4. (a) Polarization curves of CFC-600, CFC-900, NF-600, NF-900, Ni/CFC, NiΦCFC and 20 wt% Pt/C without iR correction. (b) Tafel plots derived from (a). (c,d) The DLC of CFC and PC of Ni for Ni/CFC and NiΦCFC as a function of scan rates. (e) Gibbs free energy of H* adsorption (ΔGH*) profile for the HER for various sites on NiΦCFC. (f) Chronoamperometric response for Ni/CFC and NiΦCFC at different overpotentials of 115, 215, 315, 515 mV and 565 mV. (A colour version of this figure can be viewed online.)

liquid interface, which required high sweep speeds (40, 80, 120, 160, and 200 mV s^{-1}) in a certain potential window without a faradaic process (Figs. S11a, b) and low sweep speeds (2, 5, 10, 20, and 40 mV s^{-1}) in the faradaic potential window (Figs. S11c, d), respectively. As shown in Fig. 4c and d, NiΦCFC possessed a similar DLC value of 18.3 mF cm^{-2} with that of Ni/CFC (17.9 mF cm^{-2}). However, the PC value (80.15 mF cm^{-2}) of Ni in NiΦCFC was much lower than that of Ni/CFC (213.26 mF cm^{-2}) because the increased size of Ni nanoparticles from 10 to 100 nm (600 °C, Ni/CFC, Fig. S6) to 100–300 nm (900 °C, NiΦCFC, Fig. 2). In addition, the BET specific surface area of CFC, Ni/CFC and NiΦCFC measured the N_2 adsorption-desorption method have the values of 9.073 $m^2 g^{-1}$, 166.867 $m^2 g^{-1}$ and 15.576 $m^2 g^{-1}$, respectively (Fig. S12), which confirmed the above result. Therefore, the CFC and Ni nanoparticles were not the main catalytic sites of NiΦCFC. In comparison to the loaded structure of Ni/CFC, the interface between the CFC and the Ni nanoparticles in the embedded structure of NiΦCFC significantly increased, as shown in Inset of Fig. 4d. Therefore, after ruling out the CFC and Ni nanoparticles, the increased interface between Ni nanoparticles and CFC may be responsible for the enhanced HER performance of NiΦCFC [12].

To further understand the interfacial effect between Ni and carbon, DFT calculations were used to calculate the Gibbs free energy of H* adsorption ($|\Delta GH^*|$) of different sites in NiΦCFC. To simplify the calculations, computable models of one Ni atom embedded into graphene with two types of defects (i.e., two and four carbon atoms removed) were constructed (Figs. S13a and S14a). Highly efficient HER catalysts have a $|\Delta GH^*|$ close to zero, and this value depends on the geometric and electronic structures of the catalysts [32,33]. A ΔGH^* that is too positive or too negative is detrimental to the HER because H* cannot efficiently absorb on the catalyst or desorb from the catalyst, respectively. In our DFT calculations, the large ΔGH^* values of graphene (0.73 eV, Fig. S15) and Ni atom (average value of 0.676 eV, Figs. S13b and S14b) implied that they were not the main catalytic sites of NiΦCFC. In contrast, the ΔGH^* for the interfacial carbon atoms of NiΦCFC including the ortho, meta and para carbon sites can be effectively tuned by the interfacial Ni atoms (Fig. 4e). Among the various carbon sites, the para carbon sites possessed the smallest ΔGH^* values of −0.104 eV (4-carbon defect) and 0.221 eV (2-carbon defect). However, the carbon atoms near the Ni atom (ortho sites) possessed large ΔGH^* values of −1.01 eV (4-carbon defect) and −1.176 eV (2-carbon defect), implying that the modulation of the catalytic activities required the appropriate atomic spacing between the Ni and C atoms. The larger model of six Ni atoms embedded into defective graphene by removing ten C atoms was calculated, which resulted in a similar conclusion (Fig. S16 and Table S1). Therefore, the DFT results implied that the interface between Ni and carbon with the geometric lattice defects played a fundamental role in the superior HER catalytic behaviors, which was consistent with experimental results. The established HER free-energy diagram provided a quantitative relationship between the measured electrochemical activity and theoretical ΔGH^* to further evaluate the electrocatalytic properties of the newly developed NiΦCFC in comparison with some typical metallic catalysts. The normalized experimental value of log (i_0) along with theoretically calculated ΔGH^* for NiΦCFC was marked on a volcano plot shown in Fig. S17.

The practical operation of NiΦCFC was examined using a long-term hydrogen generation experiment at high current densities. As shown in Fig. 4f, the continuous amperometric i-t testing at different overpotentials of 115, 215, 315, and 515 mV produced current densities of −7.8, −20.5, −46.2 and −147.2 mA cm^{-2} for 48 h, 48 h, 16.5 h and 113.8 h, respectively. These results indicated that NiΦCFC possessed extraordinary long-term durability. Numerous bubbles were observed on the surface of the electrodes (Fig. S18), which was confirmed to be hydrogen by gas chromatography. In contrast, the Ni/CFC decayed gradually from −74.7 mA cm^{-2} to −52.9 mA cm^{-2} with an overpotential of 565 mV in prolonged water electrolysis over 48 h (Fig. 4f). In order to explore the reason for better stability of NiΦCFC than that of Ni/CFC, after i-t testing, the according morphologies and structures were characterized. No significant changes in the morphology (SEM, Fig. S19a), crystalline phase (XRD, Fig. S19b) and elementary composition (XPS, Figs. S19c-d) of NiΦCFC were observed, confirming structural integrity as well as catalytic stability. In contrast, as for Ni/CFC, the Ni nanoparticles fell off the CFC after i-t testing (SEM, Fig. S20), leading to a dramatically diminished current density.

Therefore, the efficient HER activity as well as the good stability of NiΦCFC can be attributed to the following aspects: (i) The novel structure of the Ni nanoparticles partially embedded onto CFC increased the interface and minimized the resistance between the catalysts and the CFC substrates, leading to fast interdomain electron transport and effective electronic collection. (ii) The Ni nanoparticles were exposed to the electrolyte and contributed to the catalytic activity. (iii) The electronic density states of carbon were modulated by Ni nanoparticles, which introduced the additional catalytic activity of CFC. (iv) The embedded structure vised Ni nanoparticles, leading to the rough catalytic stability. Therefore, the superior HER activity of NiΦCFC was better than or comparable to the leading Ni metal-based HER catalysts, such as NiO/Ni-carbon nanotubes NiO/Ni-CNT (−80 mV, 51 mV dec^{-1}) [7], ultrathin nickel nanosheet array (−120 mV, 114 mV dec^{-1}) [9], thin carbon coated nickel-based nanosheets (−270 mV, 143 mV dec^{-1}) [34], NiFe-LDH/Ni foam (−210 mV) [35] and NiMo hollow nanorod array (−310 mV, 76 mV dec^{-1}) [6] (Table S2).

The use of electricity produced by solar cells to electrolyze water is a promising route for transforming distributed electrical energy into hydrogen fuels [35–37]. Here, we used a commercially available polycrystalline silicon thin film solar cell (PSSC, a maximum voltage of 2.00 V) to drive a two-electrode electrolyzer. NiFe-LDH/CFC was prepared and used as the anode for the oxygen evolution reaction (OER) [38], which was characterized by SEM (Inset of Fig. 5a) and XRD (Fig. S21). The OER polarization curves of NiFe-LDH/CFC required a overpotential of 1.49 V vs. RHE to achieve a current density of −10 mA cm^{-2} and were much better than that of NF (1.902 V vs. RHE). Based on these results, we paired up NiΦCFC as a cathode and NiFe-LDH/CFC as an anode to construct a two-electrode electrolyzer (i.e., NiFe-LDH/CFC (+)//NiΦCFC (−)) in 1 M KOH. In the dark, the electrolyzer impressively delivered a water splitting current density of −10 mA cm^{-2} at a voltage of 1.54 V (filled triangle, Fig. 5b) with vigorous gas evolution on both electrodes, which was comparable to the previously reported results, such as NiO/Ni-carbon nanotubes (1.5 V, 1 M KOH) [7], thin carbon coated nickel-based nanosheets (1.64 V, 1 M KOH) [34], NiFe-LDH/Ni foam (1.7 V, 1 M NaOH) [35], NiMo hollow nanorod array (1.64 V, 1 M NaOH) [39] and graphene/$Co_{0.85}Se$/NiFe-LDH (1.67 V, 1 M KOH) [40], as shown in Table S2. Under light illumination, a current density of 31.7 mA cm^{-2} was produced at zero voltage (hollow square, Fig. 5b). Our two-electrode electrolyzer outperformed the standard NF pair used in industrial alkaline electrolyzers, which exhibited approximately 10-fold enhancement in the dark and 4-fold enhancement under light illumination at the same voltage. In Fig. 5c, the PSSC produced a high and relatively stable current density of approximately 30 mA cm^{-2} for 9.6 h. The inset showed the actual electrolyzer for water splitting by a PSSC in sunlight, and the hydrogen production from AM 10:00 to PM 4:00 is shown in Fig. S22. The current density obtained by the PSSC was larger than that produced at 2 V in the dark (approximately 21.8 mA cm^{-2}, Fig. S23), because the current density was determined by the voltage as well as the electric quantity. The corresponding hydrogen yields were 23.7 μmol cm^{-2} h^{-1} by the PSSC (daytime) and 16.9 μmol cm^{-2} h^{-1}

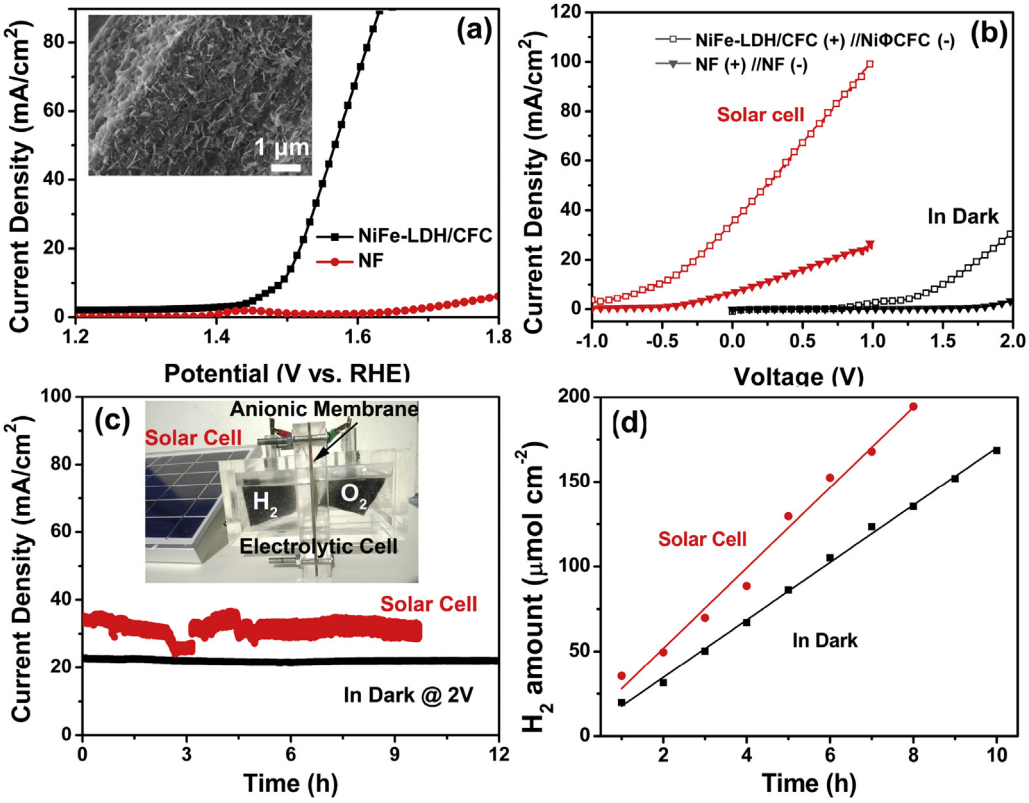

Fig. 5. (a) Polarization curves of NiFe-LDH/CFC for OER. Inset shows the corresponding SEM image. (b) Polarization curves of the alkaline electrolyzer using NiΦCFC (or NF) as the cathode and NiFe-LDH/CFC (or NF) as the anode under light illumination by a PSSC and in the dark. (c) Chronopotentiometry curves of the electrolyzer. The inset shows the actual electrolyzer using solar energy from the sun. (d) Hydrogen production as a function of time driven by PSSC (daytime) and energy storage device (night). (A colour version of this figure can be viewed online.)

by power supply (night), respectively (Fig. 5d).

4. Conclusions

Nickel nanoparticles partially embedded onto carbon fiber cloth (NiΦCFC) were simply prepared on a large scale (e.g., 40 cm × 40 cm) via a metal-mediated pitting process. The as-prepared NiΦCFC, as flexible and efficient electrodes for the HER in alkaline electrolytes, required a small overpotential of 131.5 mV to achieve −10 mA cm^{-2}. The two kinds of electrochemical area of NiΦCFC confirmed that the partially embedded structure resulted in enhanced interface effect between Ni nanoparticles and CFC substrates. The DFT results further confirmed that the para carbon atoms at the interface between Ni and carbon possessed a low Gibbs free energy of H* adsorption (|ΔGH*|), which was the most important contributor for the enhanced HER activity of NiΦCFC. Finally, the embedded structure prevented the Ni particles from falling off the CFC, leading to the long-term HER stability (no decay of −147.2 mA cm^{-2} for 113.8 h). The two-electrode electrolyzer composed of NiFe-LDH/CFC (+)//NiΦCFC (−) possessed the smallest voltage of 1.54 V (−10 mA cm^{-2}), which also can be powered by a PSSC. It is important to expect that the facile and large-scale preparation of NiΦCFC could be easily adapted for the self-powered system constituted of solar energy, electric energy and hydrogen energy.

Acknowledgements

This work was supported by Project of Public Interest Research and Capacity Building of Guangdong Province (2014A010106005), the National Key Technologies R&D Program of China (2016YFA0201104), Guangdong Innovative and Entrepreneurial Research Team Program (2014ZT05N200), Tip-top Scientific and Technical Innovative Youth Talents of Guangdong Special Support Program (2016TQ03N541), and the National Natural Science Foundation of China (51502096).

Appendix B. Supplementary data

Supplementary data related to this article can be found at http://dx.doi.org/10.1016/j.carbon.2017.07.027.

References

[1] H. Schafer, S. Sadaf, L. Walder, K. Kuepper, S. Dinklage, J. Wollschlager, L. Schneider, M. Steinhart, J. Hardege, D. Daum, Energy Environ. Sci. 8 (2015) 2685–2697.
[2] X. Jia, Y. Zhao, G. Chen, L. Shang, R. Shi, X. Kang, G.I.N. Waterhouse, L.-Z. Wu, C.-H. Tung, T. Zhang, Adv. Energy Mater. 6 (2016) 1670063.
[3] Y. Zheng, Y. Jiao, S.Z. Qiao, Adv. Mater. 27 (2015) 5372–5378.
[4] W. Zhou, J. Jia, J. Lu, L. Yang, D. Hou, G. Li, S. Chen, Nano Energy 28 (2016) 29–43.
[5] M. Gong, W. Zhou, M.J. Kenney, R. Kapusta, S. Cowley, Y. Wu, B. Lu, M.-C. Lin, D.-Y. Wang, J. Yang, B.-J. Hwang, H. Dai, Angew. Chem. 127 (2015) 12157–12161.
[6] J. Deng, H. Li, J. Xiao, Y. Tu, D. Deng, H. Yang, H. Tian, J. Li, P. Ren, X. Bao, Energy Environ. Sci. 8 (2015) 1594–1601.
[7] M. Gong, W. Zhou, M.-C. Tsai, J. Zhou, M. Guan, M.-C. Lin, B. Zhang, Y. Hu, D.-Y. Wang, J. Yang, S.J. Pennycook, B.-J. Hwang, H. Dai, Nat. Commun. 5 (2014) 4695.
[8] X. Lu, C. Zhao, Nat. Commun. 6 (2015).
[9] Y. Kuang, G. Feng, P. Li, Y. Bi, Y. Li, X. Sun, Angew. Chem. Int. Ed. 55 (2016) 693–697.
[10] Y. Li, H. Wang, L. Xie, Y. Liang, G. Hong, H. Dai, J. Am. Chem. Soc. 133 (2011) 7296–7299.

[11] D. Kong, H. Wang, Z. Lu, Y. Cui, J. Am. Chem. Soc. 136 (2014) 4897–4900.
[12] J. Deng, P. Ren, D. Deng, X. Bao, Angew. Chem. Int. Ed. 54 (2015) 2100–2104.
[13] M. Tavakkoli, T. Kallio, O. Reynaud, A.G. Nasibulin, C. Johans, J. Sainio, H. Jiang, E.I. Kauppinen, K. Laasonen, Angew. Chem. Int. Ed. 54 (2015) 4535–4538.
[14] Y. Zhou, W. Zhou, D. Hou, G. Li, J. Wan, C. Feng, Z. Tang, S. Chen, Small 12 (2016) 2768–2774.
[15] X. Zou, X. Huang, A. Goswami, R. Silva, B.R. Sathe, E. Mikmeková, T. Asefa, Angew. Chem. 126 (2014) 4461–4465.
[16] W. Zhou, T. Xiong, C. Shi, J. Zhou, K. Zhou, N. Zhu, L. Li, Z. Tang, S. Chen, Angew. Chem. 128 (2016) 8556–8560.
[17] W. Zhou, J. Zhou, Y. Zhou, J. Lu, K. Zhou, L. Yang, Z. Tang, L. Li, S. Chen, Chem. Mater. 27 (2015) 2026–2032.
[18] W. Zhou, J. Lu, K. Zhou, L. Yang, Y. Ke, Z. Tang, S. Chen, Nano Energy 28 (2016) 143–150.
[19] X. Liu, Q. Zhu, Y. Lang, K. Cao, S. Chu, B. Shan, R. Chen, Angew. Chem. 129 (2017) 1670–1674.
[20] D. Zhou, Y. Cui, P.-W. Xiao, M.-Y. Jiang, B.-H. Han, Nat. Commun. 5 (2014) 4716.
[21] P. Solís-Fernández, K. Yoshida, Y. Ogawa, M. Tsuji, H. Ago, Adv. Mater. 25 (2013) 6469.
[22] J.-S. Lee, S.-I. Kim, J.-C. Yoon, J.-H. Jang, ACS Nano 7 (2013) 6047–6055.
[23] G. Kresse, J. Hafner, Phys. Rev. B 48 (1993) 13115–13118.
[24] G. Kresse, J. Furthmüller, Comp. Mater. Sci. 6 (1996) 15–50.
[25] P.E. Blöchl, Phys. Rev. B 50 (1994) 17953–17979.
[26] G. Kresse, D. Joubert, Phys. Rev. B 59 (1999) 1758–1775.
[27] J.P. Perdew, K. Burke, M. Ernzerhof, Phys. Rev. Lett. 77 (1996) 3865–3868.
[28] H.J. Qiu, Y. Ito, W. Cong, Y. Tan, P. Liu, A. Hirata, T. Fujita, Z. Tang, M. Chen, Angew. Chem. 127 (2015) 14237–14241.
[29] H. Cao, X. Zhou, C. Zheng, Z. Liu, Carbon 89 (2015) 41–46.
[30] X. Yu, T. Hua, X. Liu, Z. Yan, P. Xu, P. Du, ACS Appl. Mater. Inter. 6 (2014) 15395–15402.
[31] H.Y. Wang, Y.Y. Hsu, R. Chen, T.S. Chan, H.M. Chen, B. Liu, Adv. Energy Mater 5 (2015) 395–417.
[32] H.J. Qiu, Y. Ito, W. Cong, Y. Tan, P. Liu, A. Hirata, T. Fujita, Z. Tang, M. Chen, Angew. Chem. Int. Ed. 54 (2015) 14031–14035.
[33] X. Cui, P. Ren, D. Deng, J. Deng, X. Bao, Energy Environ. Sci. 9 (2016) 123–129.
[34] W. Xi, Z. Ren, L. Kong, J. Wu, S. Du, J. Zhu, Y. Xue, H. Meng, H. Fu, J. Mater. Chem. A 4 (2016) 7297–7304.
[35] J. Luo, J.-H. Im, M.T. Mayer, M. Schreier, M.K. Nazeeruddin, N.-G. Park, S.D. Tilley, H.J. Fan, M. Grätzel, Science 345 (2014) 1593–1596.
[36] Z. Peng, D. Jia, A.M. Al-Enizi, A.A. Elzatahry, G. Zheng, Adv. Energy Mater 5 (2015) 1402031.
[37] R. Sathre, C.D. Scown, W.R. Morrow, J.C. Stevens, I.D. Sharp, J.W. Ager, K. Walczak, F.A. Houle, J.B. Greenblatt, Energy Environ. Sci. 7 (2014) 3264–3278.
[38] M. Gong, Y. Li, H. Wang, Y. Liang, J.Z. Wu, J. Zhou, J. Wang, T. Regier, F. Wei, H. Dai, J. Am. Chem. Soc. 135 (2013) 8452–8455.
[39] J. Tian, N. Cheng, Q. Liu, X. Sun, Y. He, A.M. Asiri, J. Mater. Chem. A 3 (2015) 20056–20059.
[40] Y. Hou, M.R. Lohe, J. Zhang, S. Liu, X. Zhuang, X. Feng, Energy Environ. Sci. 9 (2016) 478–483.